Generation of Weyl points in coupled optical microdisk-resonator arrays via external modulation

Yi Zhang and Yongyuan Zhu*

*National Laboratory of Solid State Microstructures and Collaborative Innovation Center of Advanced Microstructures
and Key Laboratory of Modern Acoustics, Nanjing University, Nanjing 210093, China
and School of Physics, Nanjing University, Nanjing 210093, China*

We theoretically propose a scheme to produce Weyl points in two-dimensional (2D) optical microdisk-resonator arrays, which undergo a dynamical modulation with temporal periodicity. By mapping the set of modes supported by each resonator to a synthetic frequency dimension, the 2D lattice is equivalent to a three-dimensional (3D) time-independent lattice. We show that, by breaking the inversion symmetry (I symmetry) or introducing artificial gauge fields, Weyl points can be formed, leading to anomalous topological edge states and Fermi arcs. This approach may provide a way to design robust topological photonic devices on chips and future applications for integrated photonics.

I. INTRODUCTION

In recent years, topological photonics has become a rapidly growing field in optics [1,2]. Analogous to topological insulators, the light in some artificial topological photonic crystals and metamaterials [3–5] shows some remarkable features. The potential applications for optical devices arouse great interest for realization of the photonic systems with topological characteristics [6–9]. Recently, a new topological material called Weyl semimetal [10,11] emerged. One important feature of the material is the appearance of Weyl points, which are similar to Dirac points but have no spin degeneracy. The dispersions close to Weyl points are governed by the Weyl Hamiltonian $H_k = \sum_{i,j} \Delta k_i v_{ij} \sigma_j$, $i,j \in \{x,y,z\}$, where $\vec{\Delta k} \equiv (\Delta k_x, \Delta k_y, \Delta k_z)$ is the displacement vector from the Weyl point and σ_j are Pauli matrices; v_{ij} characterizes a topological Chern number (topological charge) c_T of the Weyl Hamiltonian by $c_T = \text{sgn}[\det(v_{ij})] = \pm 1$. Owing to all Pauli matrices occurring in the Weyl Hamiltonian, the edge states generated are robust to impurities and defects, even for any perturbations breaking T symmetry (time symmetry) and I symmetry (inversion symmetry). Generally, due to the demand of all three Pauli matrices, the Weyl points are considered as only occurring in three-dimensional (3D) lattices. To date there are two methods to produce Weyl points in photonic systems; one focuses on I symmetry broken via designing complex 3D photonic crystal or metamaterials [12–14], the other via using gyromagnetic or gyroelectric materials and applying an external magnetic field [15]. However, for applications in micro- and nanophotonics circuits on chips, the formation of Weyl points in a two-dimensional (2D) photonic system is very attractive.

In this paper, we theoretically propose a scheme to generate Weyl points in 2D coupled disk high-Q microresonator arrays, which can be characterized by band dispersion structure of a 3D lattice. The key of the scheme is to introduce a third synthetic dimension by using a set of resonant modes with equal frequency space supported by each resonator and a

time-dependent modulation on the dielectric tensor of each resonator. Similar to a real 3D case, two methods are suggested for the formation of the Weyl points: one by making the two sublattices different to break I symmetry and the other by inducing an artificial gauge field to break I symmetry or T symmetry.

The rest of this paper is arranged as follows. In Sec. II a scheme is proposed to produce a synthetic dimension in a 2D resonator array and the general Hamiltonian of the system is provided. In Sec. III we design Weyl points in model I by making a difference between sublattice sites to break I symmetry. In Sec. IV the Weyl points are produced in model II via adding external modulation phases in resonators to introduce an artificial gauge field. In Sec. V we show the edge states and Fermi arcs in our models. In Sec. VI the Proposals for experimental realizations are discussed. In the Conclusions, Sec. VII, a brief summary of the obtained results is presented.

II. SYNTHETIC DIMENSION AND GENERAL HAMILTONIAN

We consider a 2D honeycomb lattice of disk resonators as shown in Fig. 1(a). It is noted that the structure can be seen as a triangular lattice with a basis of two "atoms" per unit cell. Therefore, without loss of generality, we distinguish between sublattices A and B with two kinds of resonators. Each resonator at A (B) supports a set of modes with their frequencies equally spaced at a frequency $\Omega^{A(B)}$, as shown in Fig. 1(b). We assume that there is only nearest-neighbor coupling between resonators in the 2D lattices, and the microresonator at sublattice site A (B) is periodically modulated at a frequency Ω, which induces coupling between modes in the same resonator at A (B) with frequencies separated by Ω. The Hamiltonian of the lattices can be written as follows:

$$
\begin{aligned}
H = &\sum_{i,l} \left(\omega_l^A a_{i,l}^\dagger a_{i,l} + \omega_l^B b_{i,l}^\dagger b_{i,l} \right) + h \sum_{\langle i,j \rangle, l} \left(a_{i,l}^\dagger b_{j,l} + \text{H.c.} \right) \\
&+ g_A \cos(\Omega t + \varphi_A) \sum_{i, \langle l,l' \rangle} \left(a_{i,l}^\dagger a_{i,l'} + a_{i,l'}^\dagger a_{i,l} \right) \\
&+ g_B \cos(\Omega t + \varphi_B) \sum_{i, \langle l,l' \rangle} \left(b_{i,l}^\dagger b_{i,l'} + b_{i,l'}^\dagger b_{i,l} \right),
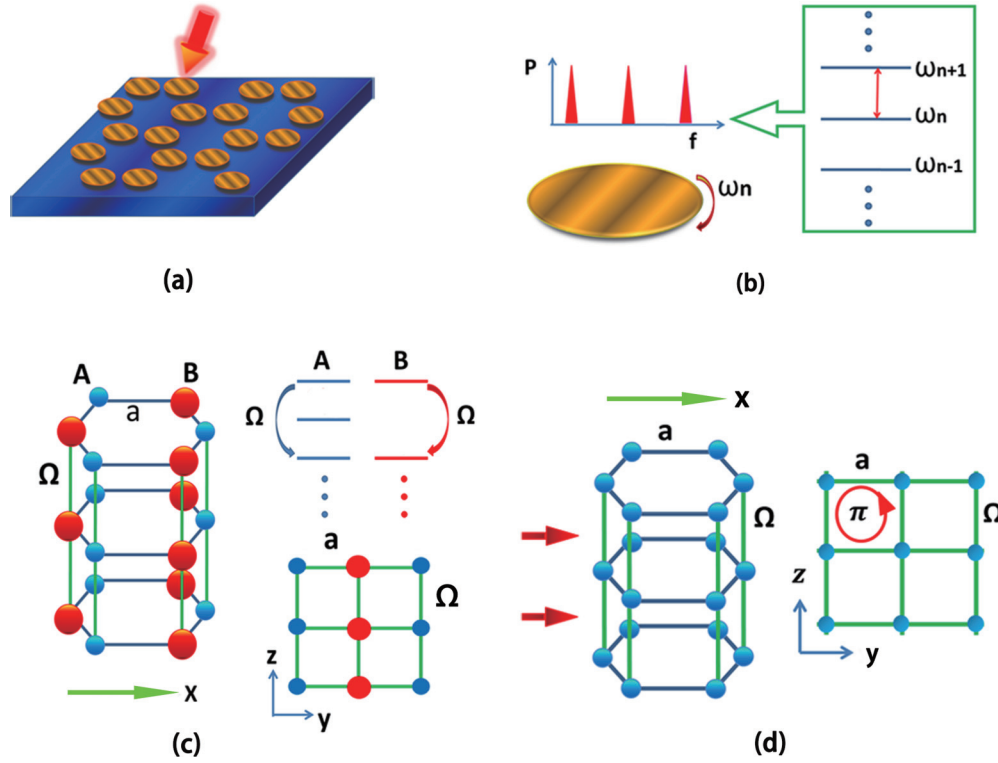\end{aligned}
\tag{1}
$$

*yyzhu@nju.edu.cn

FIG. 1. (a) Illustration of a 2D graphene-like lattice of disk resonators. (b) Each disk resonator supports a set of resonant modes with the frequencies with equal spacing (left). The discrete modes can map to a synthetic frequency dimension (right, green rectangle). (c) (Left) Model I with two different sites (small blue and large red spheres represent sublattices A and B, respectively), which breaks P symmetry in the lattice. a is the nearest-neighbor distance of the lattice and the interval in the frequency dimension equal to Ω. Here it is noted that we choose the frequency spacing of resonator B as two times that of A. (Upper right) The corresponding diagrams of the synthetic dimension of sublattice sites A and B. (Lower right) The diagram of a 2D lattice projected along the x axis. (d) (Left) Model II with identical sites and an artificial magnetic field **B** (red arrow). Here T symmetry is broken while P symmetry is preserved. (Right) The diagram of artificial magnetic field in model II. The plane projected along the x axis passed through by the artificial magnetic field. The red circle means the magnetic flux per plaquette with π. Therefore, the model is equivalent to a Harper-Hofstadter model with $\Phi = \frac{1}{2}$.

where $\omega_l^m = \omega_0^m + l\Omega^m$ [$m \in (A,B)$] gives the on-site potential for lth frequency eigenmode at the resonator on sublattice A (B); ω_0^m is the frequency of the zero-order mode (here the group velocity dispersion is neglected) and $\Omega^m = c/n_m R_m$ is the frequency spacing between adjacent modes in the resonator with effective refractive index n_m and radius R_m; $a_{i,l}^\dagger$ ($a_{i,l}$) are the creation (annihilation) operators for the lth mode of resonator at sublattice A on lattice site i [an equivalent definition of $b_{i,l}^\dagger$ ($b_{i,l}$) is used for sublattice B]; h is the coupling constant between nearest-neighbor resonator; g_A (g_B) represents the coupling constant between two modes (lth and l'th) of each resonator on sublattice A (B) with φ_A (φ_B) being the corresponding modulation phase.

Some previous works [16,17] have pointed out that a high-Q microresonator can support a set of modes with their frequencies equally spaced forming an optical frequency comb, and the set of modes can map to a synthetic one-dimensional space [18,19], as illustrated in Fig. 1(b). Thus the system we just described can be considered to be a 3D lattice model by stacking 2D graphenelike lattices layer by layer with the vertical axis corresponding to frequency. Clearly this axis can only take discrete values determined by disk-resonator modes. On the other hand, an external modulation with appropriate frequency can excite hopping between the

two modes of the set with frequency spacing equaling the frequency. Therefore, we can consider the frequency interval between two arbitrary modes of the resonator as the lattice spacing of the synthetic one-dimensional space if we choose the correct parameters of resonator and external modulation frequency.

Moving to a rotating frame by defining a transform $c_{i,l}^A = a_{i,l}e^{il\Omega^A t}$ ($c_{i,l}^B = b_{i,l}e^{il\Omega^B t}$), the Hamiltonian of Eq. (1) can be rewritten as follows:

$$
H = \omega_0^A \sum_{i,l} c_{i,l}^{A\dagger} c_{i,l}^A + \omega_0^B \sum_{i,l} c_{i,l}^{B\dagger} c_{i,l}^B + h \sum_{\langle i,j \rangle, l} \left(c_{i,l}^{A\dagger} c_{j,l}^B + \text{H.c.} \right)
$$
$$
+ g_A \sum_{i,l} \left(e^{-i\varphi_A} c_{i,l}^{A\dagger} c_{i,l+p}^A + e^{i\varphi_A} c_{i,l+p}^{A\dagger} c_{i,l}^A \right)
$$
$$
+ g_B \sum_{j,l} \left(e^{-i\varphi_B} c_{j,l}^{B\dagger} c_{j,l+q}^B + e^{i\varphi_B} c_{j,l+q}^{B\dagger} c_{j,l}^B \right), \qquad (2)
$$

where we apply the rotating wave approximation and assume that an external modulation frequency (Ω) and the adjacent modes spacing of resonators in sublattice A and B (Ω^A and Ω^B) satisfy $\Omega = p\Omega^A = q\Omega^B$ (p and q are integers), which keeps the translation invariant in the direction of the synthetic dimension.

The first line in Eq. (2) is the Hamiltonian of 2D lattices in real space with nearest-neighbor coupling, and the second and third lines describe the coupling between adjacent frequencies of sublattices A and B along the synthetic dimension,

$$H_k = \begin{bmatrix} \omega_0^A + 2g_A \cos(k_z\Omega + \varphi_A) & \rho \\ \rho^* & \omega_0^B + 2g_B \cos(k_z\Omega + \varphi_B) \end{bmatrix}, \tag{3}$$

where $\rho = e^{-ik_x a} + 2\cos(\sqrt{3}k_y a/2)e^{ik_x a/2}$, a is the distance between the two sublattices of the real 2D resonator array, and $\bar{k} \equiv (k_x, k_x, k_z)$ is the Bloch wave vector in reciprocal space of the 3D lattice. It is noted that here the lattice intervals in the synthetic dimension in the 3D model are represented by the modulation frequency Ω.

III. MODEL I WITH INVERSION SYMMETRY BROKEN

We first consider model I with inversion symmetry broken, as illustrated in Fig. 1(c) (left), which can be induced by making the frequency spacing of resonators at sublattices A and B with $2\Omega^A = \Omega^B$ via choosing the appropriate value of effective refractive index and radius of the resonators. Here, we assume the external modulation frequency satisfying $\Omega = 2\Omega^A = \Omega^B$.

The eigenvalues of H_k are given by

$$E = (\omega_0^A + \omega_0^B)/2 + (g_A + g_B)\cos k_z\Omega$$
$$\pm \sqrt{|\rho|^2 + [(\omega_0^A - \omega_0^B)/2 + (g_A - g_B)\cos k_z\Omega]^2}. \tag{4}$$

In the real 2D lattice, which hass no term of $(g_A - g_B)\cos(k_z\Omega)$, if $\omega_0^A \neq \omega_0^B$ and the first term under the square vanishes ($|\rho| = 0$), the inversion symmetry is broken, which induces a gap in band dispersion. However, in the synthetic 3D lattice of model I, the second term in the square can be equal to zero via choosing the appropriate value of Ω. More specifically, when A and B are not identical, the gap of the band dispersion can be opened in a 2D lattice at six Dirac points $(k_x, k_y) = (\pm 2\pi/3a, \pm 2\pi/3\sqrt{3}a)$ and $(0, \pm 4\pi/3\sqrt{3}a)$. However, when the modulation frequency Ω satisfying $k_z = \pm \arccos[-(\omega_0^A - \omega_0^B)/2(g_A - g_B)]/\Omega$, where $|(\omega_0^A - \omega_0^B)/2(g_A - g_B)| \leqslant 1$, this gap closes again in these points (k_x, k_y, k_z), which are denoted by red and green spheres in 3D k space [see Fig. 2(a)]. Here, the two colors (red and green) of the spheres represent positive and negative topological charges, respectively, and it is the same with model II; see Fig. 2(e). The band dispersion near the point surrounded by the red circle in the 3D k space is linear, as shown in Figs. 2(b)–2(d), indicating that the degeneracy point is a Weyl point which usually exists in a true 3D lattice band structure.

The lattice considered here has the mirror symmetry in the (x,z) plane, which ensures the topological charges of the Weyl points of (k_x, k_z) have the same signas those of $(-k_x, -k_z)$ and the net charge in the horizontal plane is zero. This can be seen from Fig. 2(a).

respectively. We can clearly see that the above Hamiltonian describes a 3D tight-binding lattice model with two sublattices. For an infinite case, Eq. (2) can be Fourier transformed into k space:

IV. MODEL II WITH ARTIFICIAL GAUGE FIELD

The other method to produce Weyl points is to introduce an external magnetic field. This can be handled according to the Hamiltonian of Eq. (3). The difference is that here we assume all the resonators are identical (we obtain $g_A = g_B \equiv g_0$) and the external modulation frequency Ω satisfies the condition $\Omega \equiv \Omega^A = \Omega^B$. The key to realizing model II is to make the phase modulation φ_A different from φ_B. Here, the frequency modulation induces a coupling between adjacent modes in each resonator, while the phase modulation can be used to achieve an artificial magnetic field. Below, we choose $\varphi_A = 0$ and $\varphi_B = \pi$. When the above conditions are satisfied, the second and third lines of Eq. (2) are analogous to **the** 2D bosonic Harper- Hofstadter (HH) model for the flux per plaquette $\Phi = \frac{1}{2}$ [20,21]. As is well known, the HH model describes the electrons in lattices with an external magnetic field. Therefore, according to the analogy it means that an effective magnetic field is artificially produced in our system along the horizontal direction as shown in Fig. 1(d) (left). As a result, it can be considered as an analog of the quantum Hall effect within the 2D rectangle lattice plane which is perpendicular to the synthetic magnetic field [Fig. 1(d) (right)]. The corresponding Hamiltonian is given by

$$H_k = \begin{bmatrix} 2g_0\cos(k_z\Omega) & \rho \\ \rho^* & -2g_0\cos(k_z\Omega) \end{bmatrix}. \tag{5}$$

We can obtain the energy band of the model II $E = \pm\sqrt{|\rho|^2 + 4g_0^2\cos^2(k_z\Omega)}$. The two bands touch at Weyl points within the first Brillouin zone at (k_x, k_y, k_z) with k_x and k_y satisfying $|\rho| = 0$ and $k_z = \pm\pi/2\Omega$. In model II, there are twelve Weyl points denoted by red and green spheres in 3D k space of Fig. 2(e) and the corresponding dispersions of the Weyl point [surrounded by a red circle in Fig. 2(e)] are shown in Figs. 2(f)–2(h). We note that the above model actually is I symmetry broken just like in model I. We can also make T symmetry broken in model II by choosing the modulated phase difference between adjacent resonators along the y axis equal to $\pi/2$. In this case, the system is described by the Harper-Hofstadter model with flux of $\frac{1}{4}$ and the modulated phases of resonators being $\pi/2$, π, $3\pi/2$, and 2π, respectively. The energy spectrum of the Harper-Hofstadter model consists of four bands. Each of the four bands is topologically nontrivial, and characterized by a nonzero Chern number. The two bands in the middle of the four touch each other at some points, which are Weyl points, whereas the top two bands as well as the bottom two bands have band gaps. For a finite lattice, the edge modes will appear and move along the frequency axis. Due to relatively complex phase modulation in the experiment, the model with T symmetry broken will not be discussed further.
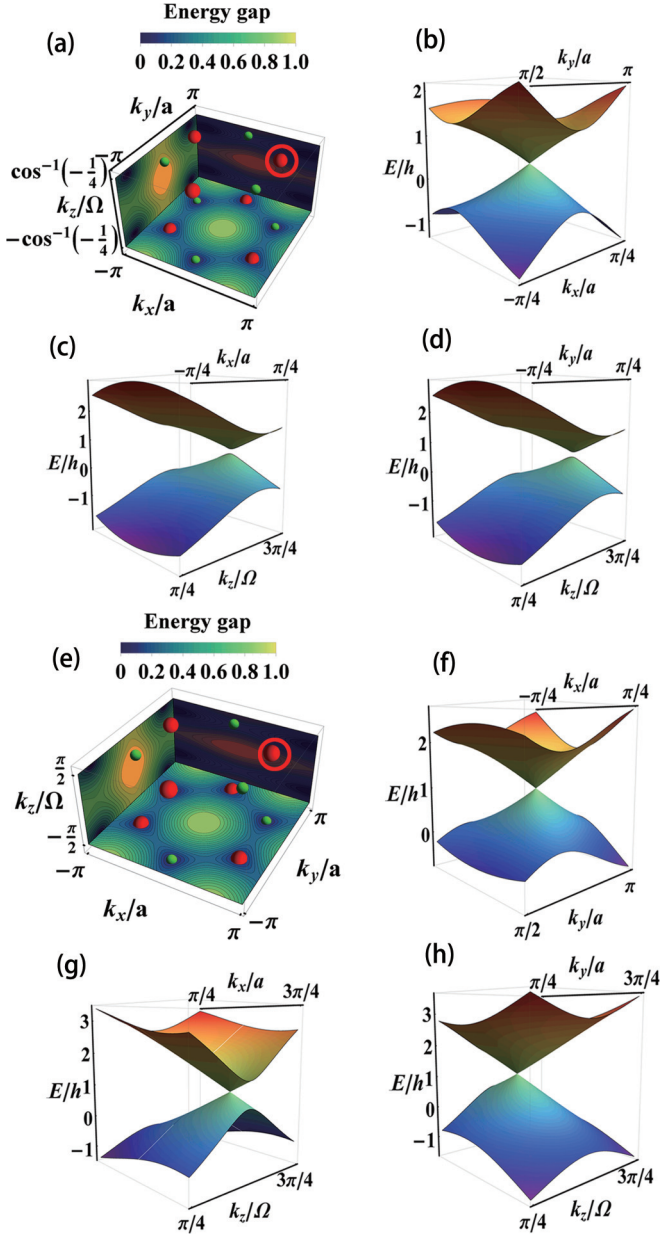
FIG. 2. Weyl points in reciprocal space of model I and model II, respectively. (a) Location of Weyl points of mode I in (k_x,k_y,k_z) space. There are 12 Weyl points in the first Brillouin zone. (b–d) The band dispersion of the Weyl point surrounded by a red circle in the left 3D diagram, i.e., the point of $[2\pi/3, 2\pi/3\sqrt{3}, \cos^{-1}(-1/4)]$. (e) Location of Weyl points of mode II in (k_x,k_y,k_z) space. Comparing with model I, the Weyl points have the same number and topological charges but different coordinates in k_z axis. (f–h) The band dispersion of the Weyl point at $(2\pi/3, 2\pi/3\sqrt{3}, \pi/2)$, which is surrounded by a red circle in the left 3D diagram. Here, large red and small green spheres denote Weyl points with positive and negative topological charge, respectively. In (a,e), the Weyl points can also be seen in three planes (k_x-k_y, k_x-k_z, k_y-k_z), which are 2D projections of Weyl points in the corresponding two k-vector components.

Here we only point out that it is the 2D generalization of the model proposed in Ref. [19] and that due to T symmetry being

broken the edge modes are topologically protected one-way modes.

In model II, the horizontal synthetic magnetic field is along the x axis; hence the mirror symmetry remains with respect to the x-z plane, so the topological charges of Weyl points in k space are the same as model I, as shown in Fig. 2(e).

V. EDGE STATES AND ANALOG OF "FERMI ARCS"

To study the edge states, we take a ribbon of our 2D lattice terminated with zigzag edges since the edge states only occur in a hexagonal ribbon with a zigzag edge. The ribbon width is 40 resonators in the transverse cross section (x direction), as Fig. 3(a) shows, while the edges are supposed to have infinite extent in the y and z direction (such that k_y and k_z are good quantum numbers). In the ordinary 2D case, the dispersion diagram of a ribbon with zigzag boundaries is shown in Fig. 3(b). Due to the flatness of the edge-mode curves, the two degenerate edge modes of the real 2D zigzag ribbon
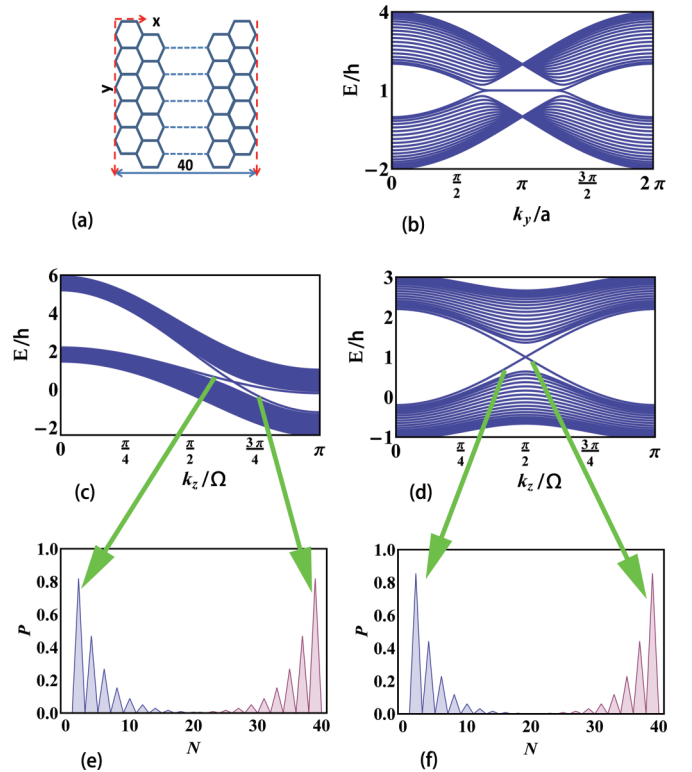

FIG. 3. (a) A ribbon of our 2D lattice with 40 resonators terminated with zigzag edges. The ribbon width is 40 resonators in the x direction. The y direction is along the red dashed line. (b) Projected band structure for 2D lattice with zigzag edge (I symmetry and T symmetry all remain). (c,d) Projected band structure for 3D lattice of model I and model II with zigzag edge in the x-z plane. The edge modes can be seen in the band gap, and the green arrowed lines indicate the intensity distribution of the edge states. (e,f) The intensity distribution diagrams of the eigenstates of the edge modes correspond to (c,d), respectively. Here, we choose $\omega_A = h$ ($\omega_B = 2h$), $g_A = 1.2h$ ($g_B = 3.2h$), and $h = \Omega$ in model I and $\omega_A = \omega_B = h$, $g_A = g_B = 1.2h$, and $h = \Omega$ in model II. It can be seen that there is one propagating edge mode in each edge of the zigzag ribbon.

are dispersionless (group velocities are zero). In other words, the edge modes do not propagate in a real ribbon and only localize in two edges. However, when we introduce the third dimension, the situation is different. This can be seen from the projected band structures along the x direction of models I and II, which are defined as the eigenvalues of Eqs. (4) and (5) with respect to the wave vector k_z [shown in Figs. 3(c) and 3(d) respectively]. Figures 3(e) and 3(f) are the intensity spectra of the eigenstates of the two models, respectively. As are shown in the two figures, the energies of the edge modes are almost completely concentrated at the edge sides of the ribbon lattice.

Furthermore, we can see from Fig. 3(c), in model I, at certain k_z the group velocities, e.g., the slopes of the two curves in gap, of the two edge modes have different magnitudes but with the same direction. For model II, at certain k_z the group velocities of the two edge states have the same magnitude but with a different direction, as shown in Fig. 3(d). The propagation of the edge modes of model I can be explained by the shape of the projected band structure in plane (E, k_x). We have found, as long as the conditions $\varphi_A = \varphi_B$ and $g_A \neq g_B$ are satisfied, the top and bottom energy bands of model I are curved with the same shape [bend upward as shown in Fig. 3(c)]. Therefore, the two edge modes bend upward as well. Here in Fig. 3(c) the slope of the top one has the same sign as the bottom one. It means that the edge modes at two boundaries in model I can move along the same direction. For model II, the case can be considered as the quantum Hall effect on the square lattice with $\Phi = \frac{1}{2}$, in which the edge modes at the two boundaries move along the opposite direction.

It should be noted that the edge modes here correspond to propagation in the frequency space, so this means that, for model I, the two edge modes $(0 < k_z < \pi)$ would cascade down in frequency at different rates as well as be confined at two boundaries of the real 2D resonator ribbon. However, in model II, due to the group velocities being equal with the opposite direction, the confined edge mode $(0 < k_z < \pi)$ at the left moves downward in frequency axis while that at the right moves upward at the same rate. For $\pi < k_z < 2\pi$, just the opposite is true. That is, frequency conversion occurs. The interaction between resonators and the external modulation field introduces transition of the edge modes up or down in frequency. The frequency conversion of the edge modes is topologically protected by Weyl points, which suggests that our setup might be used as a transducer in certain applications.

For obtaining a clear impression, we numerically simulate the frequency conversion of the edge modes shown in Figs. 4(a) and 4(b) corresponding to models I and II, respectively. To do this, we numerically solve the time-dependent Schrödinger equation,

$$i\frac{\partial}{\partial t}\psi_{r,l}^{A(B)} = -\sum_j h\left(\psi_{r-R_j,l}^{B(A)} + \psi_{r+R_j,l}^{B(A)}\right) - \Gamma_r^{A(B)}\psi_{r,l-\eta}^{A(B)}$$

$$- \Gamma_r^{A(B)*}\psi_{r,l+\eta}^{A(B)} + f_{\text{pumping}}, \quad (6)$$

where the subscript η is the hopping unit in frequency axis, $\vec{R}_j$ is the resonator position in real space, $\Gamma_r^{A(B)} = g_{A(B)}e^{-i\varphi_{A(B)}}$; f_{pumping} is the pumping term. For model I, $g_A \neq g_B$ and
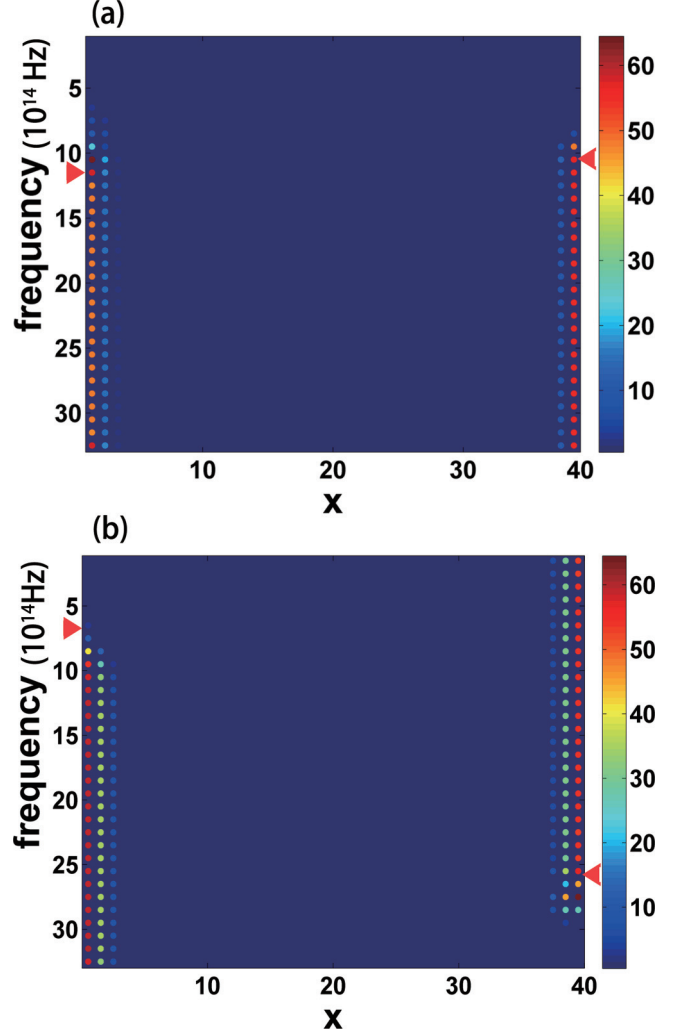

FIG. 4. Simulation of the steady-state photon-field distribution for model I and II with 40 resonators in the x axis. (a) The two edge modes of model I. Both of the two edge modes clearly propagate along the frequency axis from top to bottom. (b) The two edge modes of model II. Compared with model I, the two edge modes have opposite velocity, and the left edge mode propagates from top to bottom and the right from bottom to top. In the two figures, the resonators at the leftmost and rightmost of the x axis of the ribbon are pumped by light with a frequency marked by triangles at the frequency axis. Here, the parameters of two models are chosen to be the same as in Fig. 3 and the intensity of the pumping light is $50h$ for (a,b).

$\varphi_{A(B)} = 0$ while for model II $g_A = g_B$ and $\varphi_A = 0$, $\varphi_B = \pi$. Then we can obtain the steady-state intensity distribution $|\psi_{r,l}^{A(B)}|^2$. Here we assume the frequency axis is semi-infinite (i.e., from $l = 0$ to $l \to \infty$). Actually, in simulation we choose $l = N$ with N a larger number. The pumping lights inject at a position indicated by a triangle in the figures. The intensity of the edge modes is concentrated at both edges and propagates in the same direction of frequency axis for model I but in the opposite direction for model II, as shown in the two figures.

We note that the edge modes of the two models will only propagate in the frequency dimension, not in the real resonator array. To create propagation of the edge modes in the real

arrays, according to the method proposed in Ref. [18] we should make a hard boundary in frequency dimension. It can be realized by introducing some impurities into every disk resonator to cause great dissipation of one of modes in the disk resonators. Thus we create a sharp boundary at the mode site in frequency dimension. As a result, the edge modes can propagate along the plane perpendicular to the frequency axis. Another method is to consider the group velocity dispersion in the disk resonator [19]. The deviation between the lth mode and the sideband mode $\omega_0^m + l\Omega^m$ will be increased with the increasing of l. As a result, the coupling between the adjacent modes with higher l is missing, which is equivalent to providing a natural boundary in the frequency space. Thus the mode with frequency close to the missing mode can propagate within the real resonator arrays.

There is no deep understanding yet about the topological stability of the edge modes of the photonic Weyl system with I symmetry broken. Here we can refer to the scenario in the Weyl semimetal [22–24]. Due to a similar Hamiltonian, we think that in our case the topological protection for the edge modes follows from the separation of the Weyl points in momentum space and from the chirality of the edge modes, just like the Weyl semimetal. For model I, although the edge modes have the same chirality, the topological protection still exists as long as the Weyl points are not too close together, while for model II, the Harper-Hofstadter model with flux $\Phi = \frac{1}{2}$ and Weyl points ensures that the two topologically protected edge modes with opposite chirality are present.

In addition, we would single out that the k_z in Figs. 3(c) and 3(d) does not represent momentum. Here k_z are the reciprocal lattice vectors of frequency space and thereby represent time. With this in mind, we can avoid misunderstanding about the energy band structure of model I. As shown in Fig. 3(c), it seems that the edge modes have the same energy as some bulk modes at certain E which might lead to resonance between the edge modes and bulk modes, thereby affecting the stability of the edge modes. However, since the edge and bulk modes with the same E correspond to different k_z, it means they can only have the same energy at two different times. Therefore, for general static disorders, the edge modes cannot be resonant with the bulk modes at any time even though disorder scattering exists. However, if the disorders are time dependent, for example, with appropriate time-periodic frequency, the mixing of the modes would occur. Its physical mechanism is just like the external time-dependent modulation for the system described in Sec. II.

It is well known that the Weyl point is accompanied by the Fermi arc surface states whose dispersion curve connects two Weyl points with opposite topological charge in momentum space. We obtain the similar result in the band dispersion spectrum of this ribbon, as Figs. 5(a) and 5(b) show. For model I, the intersection of band dispersion in a projected band structure in Fig. 3(c) traces out a straight line segment terminating at the two Weyl points with opposite topological charge localized at $k_y = 2\pi/3$, $k_z = 2\pi/3$ and $k_y = 4\pi/3$, $k_z = 2\pi/3$ as k_y is varied [Fig. 5(a)]. The result for model II is shown in Fig. 5(b) with a line segment connecting two Weyl points at $k_y = 2\pi/3$, $k_z = \pi/2$ and $k_y = 4\pi/3$, $k_z = \pi/2$. The trajectories are analogous to "Fermi arcs" in electronic Weyl semimetals.

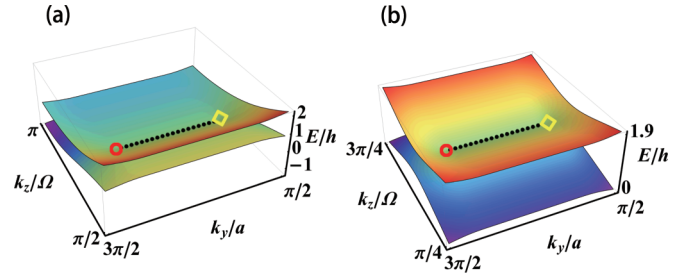

FIG. 5. The analog of "Fermi arcs" (black dotted lines in figures) in two models. The red circle (yellow diamond) denotes topological charge with $+1$ (-1). Here, the values of the parameters are chosen to be the same as Figs. 3(c) and 3(d). (a) The "Fermi arcs" in model I; (b) the "Fermi arcs" in model II.

VI. PROPOSALS FOR EXPERIMENTAL REALIZATIONS

The theoretical predictions discussed above can be realized using currently available materials and techniques.

A microresonator-based frequency comb can be produced by the interaction of a continuous-wave pump laser of a known frequency with the modes of an ultrahigh-Q microresonator via the Kerr nonlinearity [16,17]. And the fabrication techniques of high-Q microdisks arranged in well-ordered arrays over large-scale areas already exist now [25].

Beyond that, for model I we can carefully choose the radii and materials of resonators to break I symmetry as well as to make the frequency spacing between adjacent modes of resonators in sublattice A and B satisfying $p\Omega^A = q\Omega^B$ in the synthetic dimension. The coupling between lattice sites in the synthetic dimension can be realized by a change in the concentration of charge carriers via femtosecond pulsed laser pumping [26]. This can produce an ultrafast tuning of the dielectric tensor of the resonator material at a frequency that is comparable to the frequency separation of adjacent modes.

As for model II, since we assume $\varphi_A = 0$, only the phase φ_B in sublattice B should be performed by external modulation, which can be achieved by adding an electro-optic modulator at sublattice site B, in which the total electric field undergoes a modulation with specific phase and frequency [27]. Using this method, the coupling in the synthetic dimension as well as the artificial magnetic field can be realized. Alternatively, the phase φ_B can be generated by acousto-optic modulation [28], but the coupling in the synthetic dimension should be produced via an external laser pumping similar to that for model I.

VII. CONCLUSIONS

We provide a design for producing Weyl points and associated phenomena in a 2D hexagonal lattice consisting of high-Q microresonators. The 2D resonator array can be mapped to a 3D lattice model via introducing a synthetic frequency dimension. In the artificial 3D lattice, we show that Weyl points can be produced by inducing I symmetry breaking or an artificial gauge field. Thus the topological edge states and analog of Fermi arcs can be produced. The possibility of realizing the scheme by the current technique is discussed. The proposal might be useful for the study of unique topological

photonic phenomena on chips and open a way to design robust photonic devices in integrated optics.

Note added in proof. Recently, we became aware of a similar work [29]. They produce Weyl points in a 2D resonator lattice by using methods analogous to this paper and the results are consistent with ours.

[1] L. Lu, J. D. Joannopoulos, and M. Soljačić, Nat. Photonics **8**, 821 (2014).

[2] C. He, L. Lin, X. C. Sun, X. P. Liu, M. H. Lu, and Y. F. Chen, Int. J. Mod. Phys. B **28**, 1441001 (2014).

[3] M. A. Bandres, M. C. Rechtsman, and M. Segev, Phys. Rev. X **6**, 011016 (2016).

[4] V. Peano, C. Brendel, M. Schmidt, and F. Marquardt, Phys. Rev. X **5**, 031011 (2015).

[5] L. M. Nash, D. Kleckner, A. Read, V. Vitelli, A. M. Turner, and W. T. M. Irvine, Proc. Natl. Acad. Sci. USA **112**, 14495 (2015).

[6] Y. E. Kraus, Y. Lahini, Z. Ringel, M. Verbin, and O. Zilberberg, Phys. Rev. Lett. **109**, 106402 (2012).

[7] G. Q. Liang and Y. D. Chong, Phys. Rev. Lett. **110**, 203904 (2013).

[8] S. Mittal, J. Fan, S. Faez, A. Migdall, J. M. Taylor, and M. Hafezi, Phys. Rev. Lett. **113**, 087403 (2014).

[9] M. C. Rechtsman, J. M. Zeuner, Y. Plotnik, Y. Lumer, D. Podolsky, F. Dreisow, S. Nolte, M. Segev, and A. Szameit, Nature (London) **496**, 196 (2013).

[10] X. Wan, A. M. Turner, A. Vishwanath, and S. Y. Savrasov, Phys. Rev. B **83**, 205101 (2011).

[11] P. Hosur and X. Qi, C. R. Phys. **14**, 857 (2013).

[12] L. Lu, Z. Y. Wang, D. X. Ye, L. X. Ran, L. Fu, J. D. Joannopoulos, and M. Soljačić, Science **349**, 622 (2015).

[13] J. Bravo-Abad, L. Lu, L. Fu, H. Buljan, and M. Soljačić, 2D Mater. **2**, 034013 (2015).

[14] M. Xiao, Q. Lin, and S. Fan, Phys. Rev. Lett. **117**, 057401 (2016).

[15] L. Lu, L. Fu, J. D. Joannopoulos, and M. Soljačić, Nat. Photonics **7**, 294 (2013).

[16] P. Del'Haye, A. Schliesser, O. Arcizet, T. Wilken, R. Holzwarth, and T. J. Kippenberg, Nature (London, UK) **450**, 1214 (2007).

[17] T. J. Kippenberg, R. Holzwarth, and S. A. Diddams, Science **332**, 555 (2011).

[18] T. Ozawa, H. M. Price, N. Goldman, O. Zilberberg, and I. Carusotto, Phys. Rev. A **93**, 043827 (2016).

[19] L. Yuan, Y. Shi, and S. Fan, Opt. Lett. **41**, 741 (2016).

[20] D. R. Hofstadter, Phys. Rev. B **14**, 2239 (1976).

[21] P. G. Harper, Proc. Phys. Soc., London, Sect. A **68**, 874 (1955).

[22] A. A Burkov and L. Balents, Phys. Rev. Lett. **107**, 127205 (2011).

[23] B. Sbierski, G. Pohl, E. J. Bergholtz, and P. W. Brouwer, Phys. Rev. Lett. **113**, 026602 (2014).

[24] Y. Takane, J. Phys. Soc. Jpn. **85**, 124711 (2016).

[25] R. J. Zhang, S.Y. Seo, A. P. Milenin, M. Zacharias, and U. Gösele, Appl. Phys. Lett. **88**, 153120 (2006).

[26] P. Dong, S. F. Preble, J. T. Robinson, S. Manipatruni, and M. Lipson, Phys. Rev. Lett. **100**, 033904 (2008).

[27] B. E. A. Saleh and M. C. Teich, *Fundamentals of Photonics* (Wiley, New York, 1991).

[28] E. Li, B. J. Eggleton, K. Fang, and S. Fan, Nat. Commun. **5**, 3225 (2014).

[29] Q. Lin, M. Xiao, L. Q. Yuan, and S. Fan, Nat. Commun. **7**, 13731 (2016).